

UC Berkeley

UC Berkeley Previously Published Works

Title

Quantification of Arctic Soil and Permafrost Properties Using Ground-Penetrating Radar and Electrical Resistivity Tomography Datasets

Permalink

<https://escholarship.org/uc/item/9d50h19h>

Journal

IEEE Journal of Selected Topics in Applied Earth Observations and Remote Sensing, 10(10)

ISSN

1939-1404

Authors

Lger, Emmanuel
Dafflon, Baptiste
Soom, Florian
et al.

Publication Date

2017

DOI

10.1109/jstars.2017.2694447

Peer reviewed

Quantification of Arctic Soil and Permafrost Properties Using Ground-Penetrating Radar and Electrical Resistivity Tomography Datasets

Emmanuel Leger, Baptiste Dafflon, Florian Soom, John Peterson, Craig Ulrich, and Susan Hubbard

The authors are with the Lawrence Berkeley National Laboratory, Berkeley, CA 94720 USA (e-mail: eleger@lbl.gov; bdafflon@lbl.gov; flosoom@lbl.gov; jepeterson@lbl.gov; culrich@lbl.gov; sshubbard@lbl.gov).

Abstract:

Improving understanding of Arctic ecosystem climate feedback and parameterization of models that simulate freeze-thaw dynamics require advances in quantifying soil and snow properties. Due to the significant spatiotemporal variability of soil properties and the limited information provided by point-scale measurements (e.g., cores), geophysical methods hold potential for improving soil and permafrost characterization. In this study, we evaluate the use of a ground-penetrating radar (GPR) to estimate thaw layer thickness, snow depth, and ice-wedge characteristics in an ice-wedge-dominated tundra region near Barrow, AK, USA. To this end, we analyze GPR and point-scale measurements collected along several parallel transects at the end of the growing season and the end of frozen season. In addition, we compare the structural information extracted from the GPR data with electrical resistivity tomography (ERT) information about ice-wedge characteristics. Our study generally highlights the value of GPR data collected in the frozen season, when conditions lead to the improved GPR signal-to-noise ratio, facilitate data acquisition, and reduce acquisition-related ecosystem disturbance relative to growing season. We document for the first time that GPR data collected during the frozen season can provide reliable estimates of active layer thickness and geometry of ice wedges. We find that the ice-wedge geometry extracted from GPR data collected during the frozen season is consistent with ERT data, and that GPR data can be used to constrain the ERT inversion. Consistent with recent studies, we also find that GPR data collected during the frozen season can provide good estimates of snow thickness, and that GPR data collected during the growing season can provide reliable estimate thaw depth. Our quantification of the value of the GPR and ERT data collected during growing and frozen seasons paves the way for coupled inversion of the datasets to improve understanding of permafrost variability.

Abstract:

Improving understanding of Arctic ecosystem climate feedback and parameterization of models that simulate freeze-thaw dynamics require advances in quantifying soil and snow properties. Due to the significant spatiotemporal variability of soil properties and the limited information provided by point-scale measurements (e.g., cores), geophysical methods hold potential for improving soil and permafrost characterization. In this

study, we evaluate the use of a ground-penetrating radar (GPR) to estimate thaw layer thickness, snow depth, and ice-wedge characteristics in an ice-wedge-dominated tundra region near Barrow, AK, USA. To this end, we analyze GPR and point-scale measurements collected along several parallel transects at the end of the growing season and the end of frozen season. In addition, we compare the structural information extracted from the GPR data with electrical resistivity tomography (ERT) information about ice-wedge characteristics. Our study generally highlights the value of GPR data collected in the frozen season, when conditions lead to the improved GPR signal-to-noise ratio, facilitate data acquisition, and reduce acquisition-related ecosystem disturbance relative to growing season. We document for the first time that GPR data collected during the frozen season can provide reliable estimates of active layer thickness and geometry of ice wedges. We find that the ice-wedge geometry extracted from GPR data collected during the frozen season is consistent with ERT data, and that GPR data can be used to constrain the ERT inversion. Consistent with recent studies, we also find that GPR data collected during the frozen season can provide good estimates of snow thickness, and that GPR data collected during the growing season can provide reliable estimate thaw depth. Our quantification of the value of the GPR and ERT data collected during growing and frozen seasons paves the way for coupled inversion of the datasets to improve understanding of permafrost variability.

Index Terms—Arctic, electrical resistance measurement, geophysical measurements, ground penetrating radar

Introduction

The Arctic tundra ecosystem is recognized as a large source of uncertainty in quantifying feedback to global climate warming [1]. Improved prediction of Arctic ecosystem feedback often necessitates hydrothermal models that simulate freeze-thaw cycles. These models require spatially distributed estimates of active layer and permafrost volumetric fractions of water, ice, organic, and mineral components, as well as their changes over time. Core drilling and analysis can provide information about active layer and permafrost properties, but this approach is typically expensive and provides only limited spatial and temporal resolution. Merging several sources of information, including point-scale measurements (e.g., cores) and *in situ* geophysical measurements, can improve the spatial and temporal resolution of subsurface properties and structure. This is needed for understanding the Arctic ecosystem at different scales and especially through time.

A ground-penetrating radar (GPR) has been used to characterize various aspects of Arctic permafrost environments, including the estimation of thickness and dielectric properties of thaw layer [2], [3], the delineation of permafrost zones and variations in quantities and types of ground ice [4], and the identification of ice wedges [5]–[9]. Other studies have explored the

influence of freeze-thaw dynamics on the GPR signal [10]. The GPR has been used to image the interface between organic-rich and mineral soil and between high and low porous materials [11], [12]. Finally, several studies have used the GPR to map or estimate snow thickness and associated snow water equivalent [10], [13], [14].

The electrical resistivity tomography (ERT) can be used to provide information about the variations in subsurface electrical conductivity (the ability of the subsurface to conduct an electrical current) or its inverse, electrical resistivity (ohmmeter). In general, ground ice is electrically resistive, which can provide a good target for electrical imaging. Several field studies involving electrical measurements have shown the potential for characterizing the electrical conductivity distribution within a permafrost system (e.g., [15]-[17]).

The GPR and ERT sense the subsurface differently. GPR reflections emanate from interfaces between units having different dielectric permittivities, while the ERT senses the resistivity of the ground over a subsurface volume. Because these two methods have different sensitivities to conductivity and permittivity, they are complementary to each other. In the field case presented here, the bulk electrical resistivity imaged by the ERT is primarily indicative of changes in the water content in the thaw layer and of changes in soil/fluid salinity in the permafrost. The GPR is more directly sensitive to sharp boundaries in the subsurface, such as the interface between unfrozen and permafrost layers, and between permafrost and ice wedge. Permafrost characteristics and freeze-thaw processes are strongly linked to the ice-content distribution as well as the soil salinity and unfrozen water content. Thus, understanding permafrost characteristics to improve freeze-thaw predictive understanding can benefit from multiple methods that have different sensitivity, such as, for example, ERT and GPR.

While most of the GPR studies in the Arctic have investigated spatial variability in active layer thickness (ALT) and associated properties, a very limited number have focused on temporal variability at the field scale [8], [18]. Similarly, while several studies have imaged the presence of ice wedges [5]-[9], few have investigated how to extract quantitative information about ice-wedge dimensions from field data. Unfortunately, the lack of reliable ice-wedge dimension determination hinders our understanding of how important these ice features are to different processes. Ice-wedge evolution affects the local ecosystem behavior, particularly through its control on geomorphology [19], evaporation [20], and hydrological conditions [21], [22].

As part of the Next-Generation Ecosystem Experiments (NGEE-Arctic) project, we investigated the influence of freeze-thaw cycles on the GPR signal at the field scale and explored what type of information can be quantitatively and reliably extracted from GPR data in polygonal-shaped Arctic tundra. At the NGEE-Arctic Barrow, AK, field study site, GPR data were

acquired along several parallel transects at different times during the freeze-thaw cycle, together with point-scale measurements (such as snow and thaw layer thickness measurements). ERT data were also acquired along the same transects at the end of the growing season. Here, we define the growing season, the period when the thaw layer is completely thawed, and the frozen season, when the active layer is completely frozen. In this study, analysis of GPR data was performed to extract estimates of snow, soil, and permafrost properties and to evaluate the misfit between probe-measured and GPR-measured properties. Through data analysis and forward modeling, we evaluated the influence of soil physical properties and freeze state on the GPR signatures and explored the ability to extract quantitative information about ice-wedge characteristics. Finally, we explored the value of using GPR-derived information to constrain and improve ERT inversions.

SECTION II.

Site Background

The study site is located near the village of Barrow on the Alaskan Arctic Coastal Plain, approximately 6.5 km from the Beaufort Sea. The landscape at the site has a low topographic relief, varying between 2 and 6 m in elevation. The site is dominated by different types of geomorphological features including high-, low-, and flat-centered polygons [3], [7], [23], which govern the microtopography and surface hydrology. The annual air temperature varies between -30°C and $+8^{\circ}\text{C}$. The near-surface soil temperature fluctuates between -22°C and $+5^{\circ}\text{C}$, whereas at a 3-m depth, the temperature fluctuates between -12°C and -5°C . The thickness of the seasonally thawed active layer at the site is generally less than 0.5 m [3], [23]. The sediments underlying the active layer consist of a mixture of sand, silt, and gravel. These sediments are part of the Barrow unit (Gubik Formation), which is 36 m thick and generally of marine origin, with the uppermost sediments characterized by lacustrine and fluvial deposits. Postdepositional freezing occurred in several steps, likely after a process known as soil water freshening [24]. The volume of shallow ground ice around Barrow is high and predominantly associated with ice wedges and soil cryogenic structures, including segregated and pore ice.

Dafflon *et al.* [23] provides information about lateral and vertical variability of soil and permafrost properties at this site. Core samples analysis shows up to 80% ice content near the upper part of the permafrost, starting from 0.6 m below the ground surface. They identified a general decrease in the ice content with depth, leading to 45% ice at 3.5 m below the ground surface. In the same depth interval, salinity of the total water content increases from 1.4 to 41 mS/cm at 3.5-m depth. The salinity and the ice content are negatively correlated. The exception is in ice wedges, where the salinity is very low and relatively constant with depth. While the increase in the fluid salinity with depth occurs everywhere on the site, its gradient is quite variable. The organic component of the active layer is about 0.1 m thick, and

the underlying increase in the mineral content is gradual. From top to bottom of the active layer, the organic content decreases from ~90% to 10%, mineral fraction increases from 2% to 40%, and porosity decreases from 85% to 50%. Particle size analysis shows, on average, fraction about 53% of sand, 28% of silt, and 19% of clay.

Some of the lateral variations in intrinsic soil properties inside a polygon are linked to the presence of nonsorted circles that generally have higher mineral fraction and reduced organic content and porosity. At this site, they are circular-like shaped features without a stone border, but with a vegetation border. The soils within the circles are usually fine-grained, such as silt and clay, and can sometimes contain few coarse-grained soils, explaining why they are more conductive electrically than their surroundings. The growing season water content can vary significantly in the top 10 cm of the active layer, but tends to be relatively close to saturation at the base. The lowest active layer water content values are encountered at the top of high-centered polygons and on polygon rims.

SECTION III.

Data Acquisition and Processing

A. Ground-Penetrating Radar

GPR data were collected in a 2-D grid along parallel transects, which were 27.5 m long and covered a 12-m-wide area. This 2-D grid was surveyed four times from September 2012 to September 2015. To investigate the information content of the GPR as a function of the freeze state, we concentrate herein on the data collected during September 2012 and May 2013, or at the end of the growing season (deepest thaw layer equivalent to the ALT) and at the end of frozen season (frozen active layer), respectively. Consistency between datasets collected at the same time of the year but during different years is high. Common offset data were collected with Mala Ramac antennas centered at 500 MHz with a 0.06-m spacing between each trace and with a temporal sampling of 0.1 ns. Common midpoint (CMP) data were collected with the same system using 10-cm increments. In September 2012, GPR data were acquired along nine parallel transects spaced 1.5 m apart. Point-scale measurements of thaw layer thickness were also collected using a tile probe along two of these transects (6 and 9). Details on the tile probe measurement method can be found in [25]. During the May 2013 campaign, GPR data were acquired along 17 parallel transects spaced 0.75 m apart (including along the same nine transects used during the September 2012 campaign). Point-scale measurements of snow thickness were collected along two transects (6 and 9). Datasets collected along transect 6 and 9 are presented in Figs. 1 and 2, respectively. While GPR and point-scale measurements along this grid are presented here for the first time, details about other measurements at the NGEE site can be found in [23] and [3].

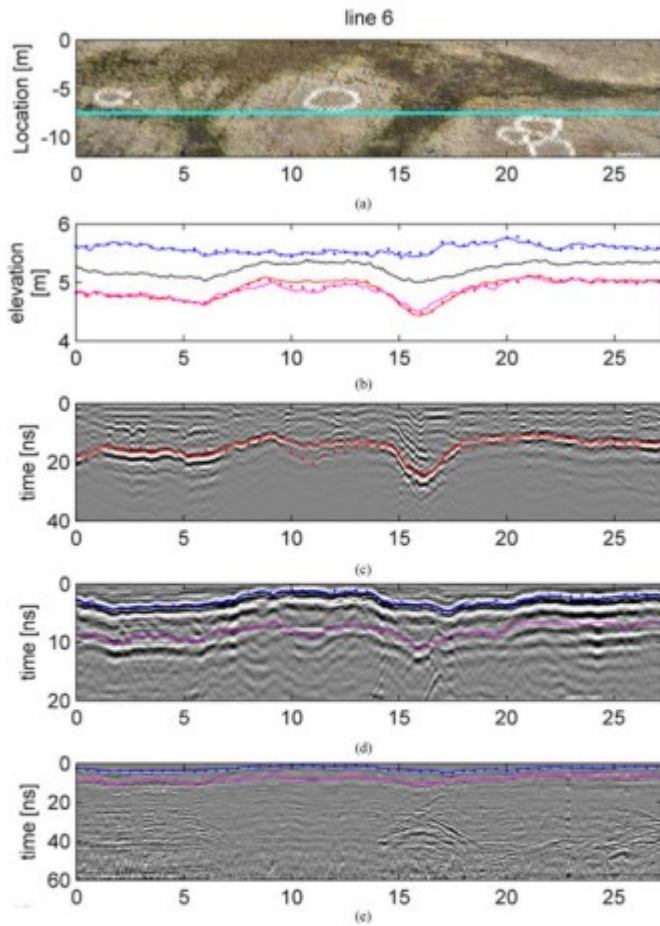


Fig. 1. (a) Plan view image of polygon ground surface showing location of GPR transect #6 (cyan line) on aerial image with nonsorted circles shown in white, (b) elevations of top of snow from probe (blue dots) and GPR (blue line) data, ground (black line), base of thaw layer from probe (red dots) and GPR (red line) data in September 2012, and base of active layer from GPR data (pink line) in May 2013, (c) radargram with base of thaw layer from probe (dots) and GPR (line) data (September 2012), (d) radargram with base of snow (blue) and active layer (purple) from probe (dots) and GPR (line) data (May 2013), and (e) same as (d) but with larger time windows and deconvolution applied.

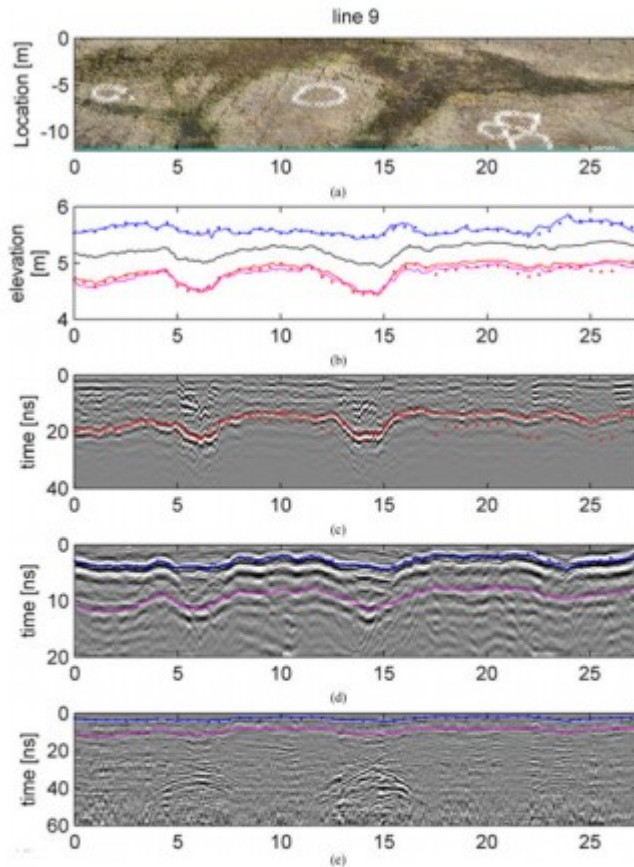


Fig. 2. (a) Plan view image of polygon ground surface showing location of GPR transect #9 (cyan line) on an aerial image with nonsorted circles shown in white, (b) elevations of top of snow from probe (blue dots) and GPR (blue line) data, ground (black line), base of thaw layer from probe (red dots) and GPR (red line) data in September 2012, and base of active layer from GPR data (pink line) in May 2013, (c) radargram with base of thaw layer from probe (dots) and GPR (line) data (September 2012), (d) radargram with base of snow (blue) and active layer (purple) from probe (dots) and GPR (line) data (May 2013), and (e) same as (d) but with larger time windows and deconvolution applied.

GPR data processing included zero-time adjustment, bandpass filtering, and gapped Wiener filtering. The two way travel times of the electromagnetic wave reflected at the bottom of thaw layer in the growing season and bottom of snow and of active layer in the frozen season were picked semiautomatically. Conversions of the picked travel times to the interfaces between the thaw, snow, and active layer compartments were based on the analysis of several CMP profiles collected at various locations on site. The time-to-depth conversion for the underlying permafrost was based on velocity retrieved from CMP hyperbola fitting. All the processes were realized through Seismic Un*x [26].

Modeling was performed to understand the GPR signature of the ice wedge and active layer under different conditions, namely the frozen season (very resistive environment) and the growing season (dispersive environment due mainly to presence of water in the thaw layer and very strong reflection from

the top of the permafrost). GPR data were simulated using the GprMax code [27], [28], which uses finite-difference time-domain modeling to solve Maxwell's equations in two or three dimensions. The GPR antennas were considered as dipoles, emitting a Ricker wavelet centered on 500 MHz in the air. The synthetic radargram shown in Fig. 3(a) represents a 0.4-m-deep frozen active layer having a relative dielectric permittivity of 7. The ice wedge is 0.2 m deeper than the base of the active layer and has a triangular symmetrical [see Fig. 3(a)] and asymmetrical [see Fig. 3(c)] shape with its lowest point at 2-m depth. Its relative dielectric permittivity was set to the value for ice. The synthetic radargram presented in Fig. 3(b) represents the growing season case, where the active layer is thawed almost through its base. The permittivity of the thaw layer was set using the Peplinski soil model [29] with percentage of sand and clay ranging from 0% to 50% and the volumetric water content from 0.05 to 0.3 cm³/cm³.

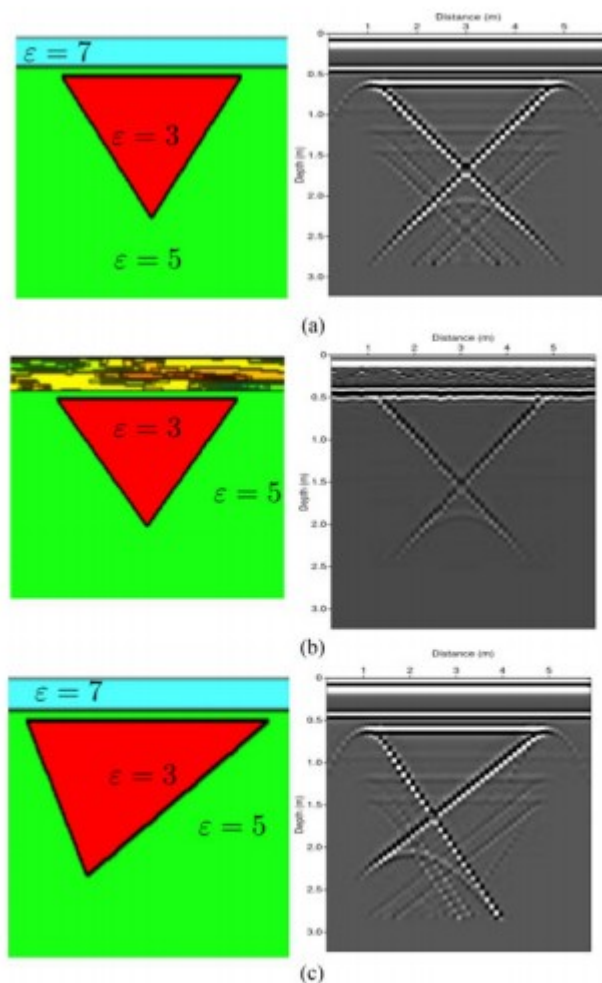


Fig. 3. Synthetic examples of GPR signal response to ice wedges including dielectric permittivity (ϵ) models (left column) and resulting radargrams (right column). The depth scale applied for the radargrams is the same as for the models. (a) and (c) represent frozen season cases and (b) growing (thawed) season case.

B. Electrical Resistivity Tomography

During the September 2012 campaign, ERT data were acquired along each of the nine transects in the grid with 0.5-m electrode spacing and a dipole-dipole array. The bulk resistivity distribution along the transects was inferred through a smoothness-constraint inversion. Topography and aerial-based imaging were performed using a camera mounted on a kite-based platform and ground control points surveyed with the real-time kinematic differential global positioning system and reconstructed using the structure-from-motion technique. The map is presented in Figs. 1(a) and 2(a). While we concentrate on the ERT data collected along lines 6 and 9, a full pseudo 3-D reconstruction of the ERT grid can be found in [23]. In comparison with the work presented in [23], here, we investigate the use of structural constraints extracted from GPR data to constrain the ERT inversion.

ERT data were inverted using boundless electrical resistivity tomography (BERT) code [30], [31], a finite-element-based inversion process. All the other processes were handled through MATLAB/Unix scripting. The finite-element meshes were generated using GMSH [32], Tetgen [33], and Triangle [34]. The topography was incorporated in all inversions.

SECTION IV.

Results

A. GPR Field Data

The GPR field data were acquired in order to estimate active layer depth and ice features such as ice wedges. In the growing season, the thaw layer velocity was estimated to be 0.045 ± 0.005 m/ns. In the frozen season, the top reflector was identified as the base of the snow layer and the second one as the base of the active layer. The velocity of snow and frozen active layer were estimated as 0.25 ± 0.01 m/ns and 0.134 ± 0.005 m/ns, respectively. The GPR-estimated depths to reflectors were compared to tile probe measurements (see Fig. 4). The frozen season GPR dataset was also used to evaluate locations and characteristics of ice wedges by investigating associated hyperbolic reflections [see Figs. 1(e) and 2(e)]. Due to the high signal-to-noise ratio, a 3-D reconstruction was possible using the frozen season dataset. Fig. 5 displays four horizontal time slices extracted from the 3-D reconstruction. These slices clearly show the base of the snow layer thicker around the polygon [see Fig. 5(b)], the base of the active layer [see Fig. 5(c)], the network of ice wedges [see Fig. 5(d)], and the depth reached by the deepest ice wedges [see Fig. 5(e)]. Fig. 5(a) and (f) shows vertical slices, corresponding to the sides of the 3-D reconstruction (line 1, corresponding to 0 m and line 9 corresponding to 12 m).

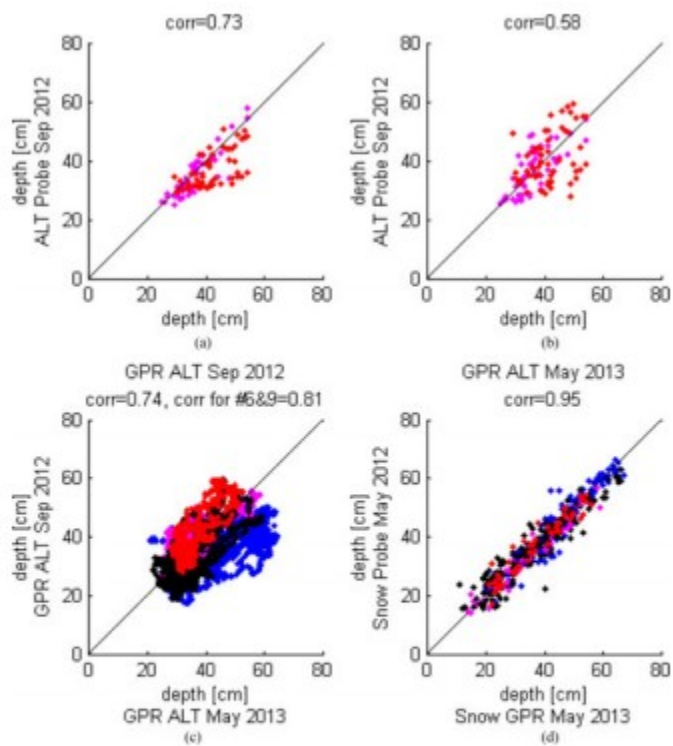


Fig. 4. Cross-plot and R^2 correlation coefficient between probe-measured ALT and GPR-estimated ALT in (a) September 2012 and (b) May 2013. (c) Cross-plot and R^2 correlation coefficient between GPR-estimated ALT in September 2012 and May 2013, and (d) between probe-measured and GPR-estimated snow layer thickness. Data are from transect 1 to 5 (blue), 6 (purple), 7–8 (black), and 9 (red).

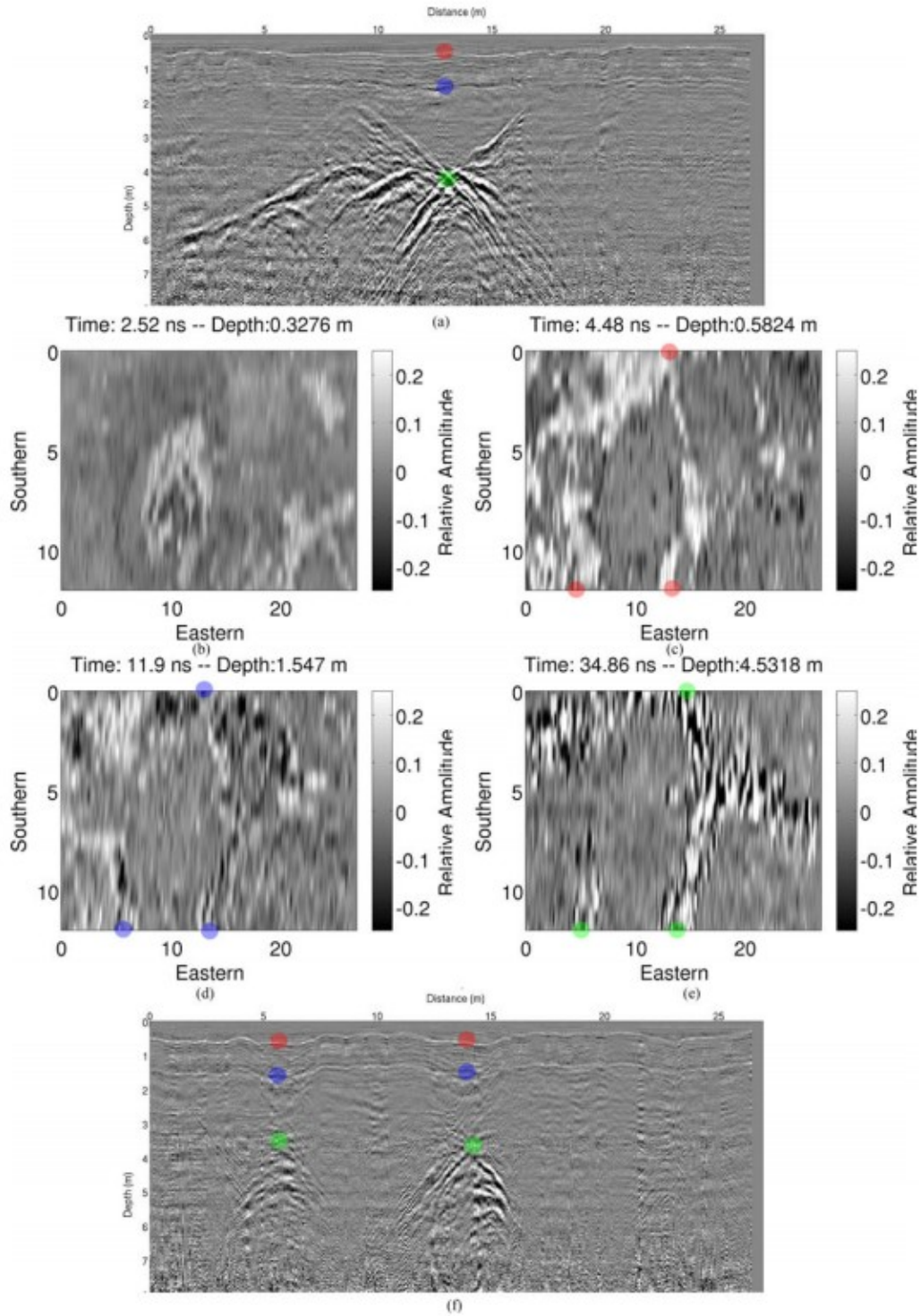


Fig. 5. (a) GPR profile for line 1, corresponding to 0 m. The y -axis is converted depth in meter, and the x -axis is the distance in meter. (b)–(e) represent time slices at different two way travel times (or depth). The slices have been processed by interpolating the 17-line radargrams, separated by 0.75 m each. (f) is line-9 radargram, corresponding to 12 m. The dots are used for linking remarkable reflections between the different radargrams in the cross-sectional plane [radargrams (a) and (f)] and in the surface view plane [radargrams (b)–(e)]. Red dots are at 0.58 m, blue dots are at 1.547 m, and green dots are at 4.53 m deep.

The 3-D distribution of ice wedges is clearly visible in the frozen season GPR dataset (see Figs. 1(e), 2(e), and 5). Although not shown, identification of 3-

D ice-wedge geometry was much more difficult using the growing season GPR data [see Figs. 1(c) and 2(c)]. This is due to the relatively lower attenuation of the GPR signal in the active layer when it is entirely frozen as well as the higher amount of energy transmitted from the base of the active layer into the permafrost under frozen conditions even when some of this energy is lost in the reflection at the snow-ground interface.

The GPR data collected in September 2012 confirm that GPR provides good estimates of thaw layer thickness using a constant GPR velocity (see Figs. 1– 5). The correlation coefficient between probe-measured and GPR-estimated thaw layer thickness is about 0.73 [see Fig. 4(a)]. The misfit is primarily related to the spatial variation in soil water content and physical properties. In fact, the largest discrepancy between probe-measured and GPR-estimated values is related to the presence of small nonsorted circles shown with white crosses in Figs. 1(a) and 2 (a). Although it does not seem to be the case here, discrepancy between probe-measured and GPR-estimated thaw layer thicknesses has also been observed in the presence of deep ponds in low-centered polygon areas, where variable permittivity and antenna coupling is also common [35]. The GPR data collected in May 2013 confirm that in addition to providing accurate estimate of snow layer thickness [see Fig. 4(d)], such data contain a fairly horizontal continuous reflector (not a multiple) as well as reflections and hyperbolas related to ice wedges [see Figs. 1 and 2 and especially Fig. 5(a) and (f)]. The value of using GPR for snow thickness estimation is shown by the correlation coefficient of 0.95 between probe-measured and GPR-estimated snow layer thickness [see Fig. 4(d)]. The deeper reflector identified in the frozen season GPR data is related to the relatively sharp increase in ice-content between the bottom of the active layer and the top of permafrost. The estimated depth to this reflector is consistent with the measured and estimated thaw layer thickness along lines 6 and 9 in September 2012 [see Figs. 1(b) and 2(b)], which can be considered equivalent to the ALT since the data were collected at the end of the growing season.

B. GPR Numerical Study

To further investigate the GPR signal response to the presence of ice wedges during the growing season and frozen season conditions, we compared field data described above to synthetic results. The objective were to explore the type of information that can or cannot be extracted from the GPR data, especially with regard to ice-wedge shape and location. The synthetic radargram shown in Fig. 3 illustrates that the bottom of the active layer as well as the triangular sides of the ice wedge are clearly identifiable. The bottom hyperbola results from the diffracting point at the bottom corner of the triangular ice wedge. Despite the very simple model, the hyperbola and side reflections are evident on the field data, more particularly in the frozen season data (see Figs. 1(e), 2(e), and 5). The synthetic radargram presented in Fig. 3(b) represents the growing season case, where the active layer is thawed almost through its base. Clearly, the ice-wedge limits are more

difficult to identify on the real data due to the scattering of the electromagnetic signal. As the modeling also shows, the influence of the fine layer of silt above the ice wedge has a critical influence on the data quality. The modeling results are consistent with our experience that it is difficult to extract information about ice-wedge geometry from GPR data collected during the growing season. The last synthetic radargram case [see Fig. 3(c)] represents an asymmetrical ice wedge, where the right side of the triangle reflects more energy to the receiver, giving the impression that the interface is not the same (in terms of permittivity gradient) as the left side. This modeling result can be used to interpret (for example) the frozen season GPR data along line 9 [see Fig. 2(e)], where one of the possible explanations for the event between 15 and 20 m and 30 and 40 ns could be the shape of the ice wedge and the direction in which the ice wedge is traversed.

C. ERT-Field data Inversion

Line 6 and line 9 data were inverted using BERT with a mesh generated with GMSH. Three different inversion case studies were performed to investigate the benefit of incorporating structural information extracted from GPR data. The first case study did not involve any *a priori* constraint on the inversion mesh. The second case study involved *a priori* constraints on the mesh by defining a mesh boundary at the bottom of the thaw layer. The third case study also included a constraint on the position and size of the ice wedge.

The active layer depth and the ice-wedge characteristics were both retrieved from the GPR data. Extraction of ice-wedge characteristics involved hyperbola fitting at 14 m along GPR transect 6, where the transect crosses the ice-wedge perpendicularly, leads to an estimate of the ice-wedge vertical thickness of about 0.98 m for line 6 and 1.9 m for line 9. The lateral extent of the ice wedge extracted from GPR data is 2.7 m, which is similar to the width of the trough (2.5 m if referring to the trough floor and 3.5 m if measuring trough from the middle of rim height). The lateral extent of the ice wedge extracted from GPR data along line 9 is 3.7 m, which is also relatively close to the width of the trough (3.5 m if referring to the trough floor and 4.0 m if measuring trough from the middle of rim height). This means that lateral extent of ice wedge can be inferred from digital elevation models, which can be obtained using aircraft, unmanned aerial vehicles, or as in this case, a kite.

The inverted ERT data along line 6 and line 9 are shown in Figs. 6 and 7, respectively. Fig. 8 shows a sensitivity analysis to complement results shown in Fig. 6. The three case study inversions are compared along line 6 (see Fig. 6) and line 9 (see Fig. 7). The statistics on the misfit between simulated and measured data are presented in Tables I and II for lines 6 and 9, respectively. The first row of both tables provides the statistical parameters quantifying the misfit resulting from the ERT data inversion for a nonconstrained mesh. These results are illustrated in Figs. 6(a) and 7(a) for lines 6 and 9, respectively. The second row of Tables I and II represents a

constrained mesh inversion, where the active layer depth obtained through GPR data has been used to constrain the mesh. These results are illustrated in Figs. 6(b) and 7(b) for lines 6 and 9, respectively. The third row of Tables I and II represents a constrained mesh inversion, where the active layer depth and the ice-wedge position obtained through GPR data have been used to constrain the mesh. These results are illustrated in Figs. 6(c) and 7(c) for lines 6 and 9, respectively.

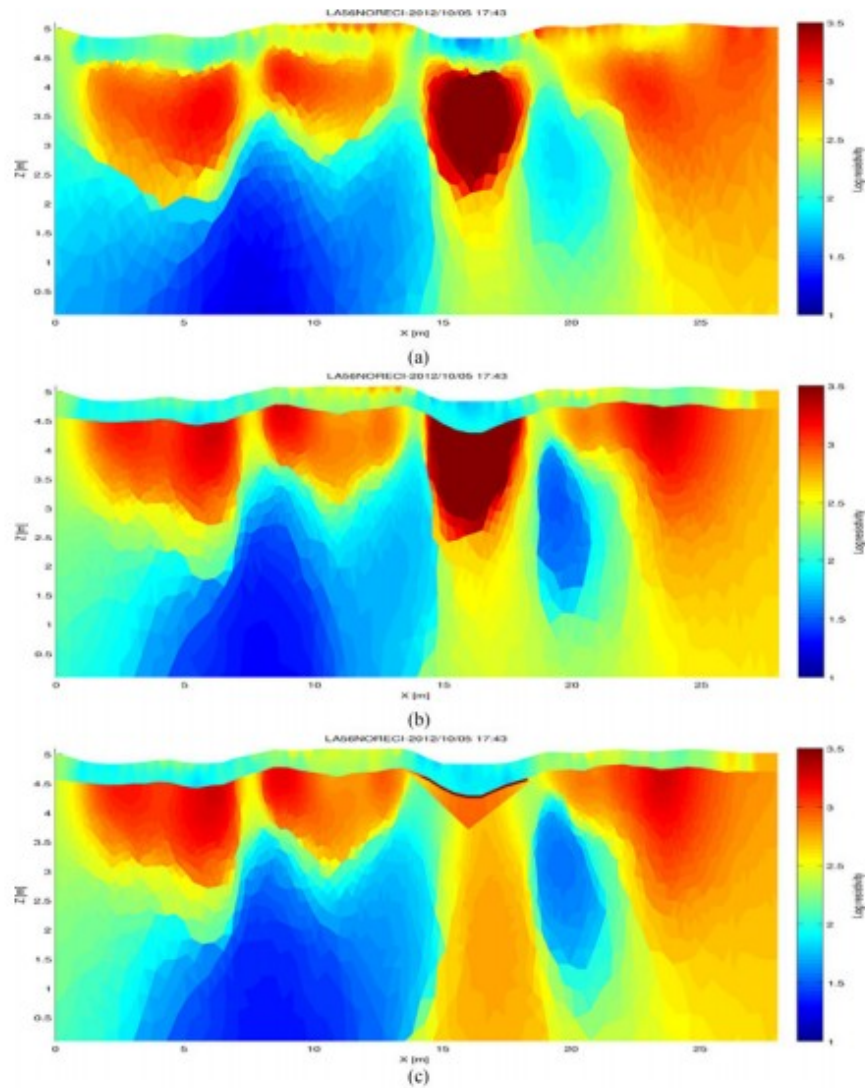


Fig. 6. Line 6 inverted bulk resistivity (ohmmeter) displayed with \log_{10} scales. (a) Unconstrained inversion. (b) Active layer mesh-constrained inversion. (c) Active layer and ice-wedge mesh-constrained inversion.

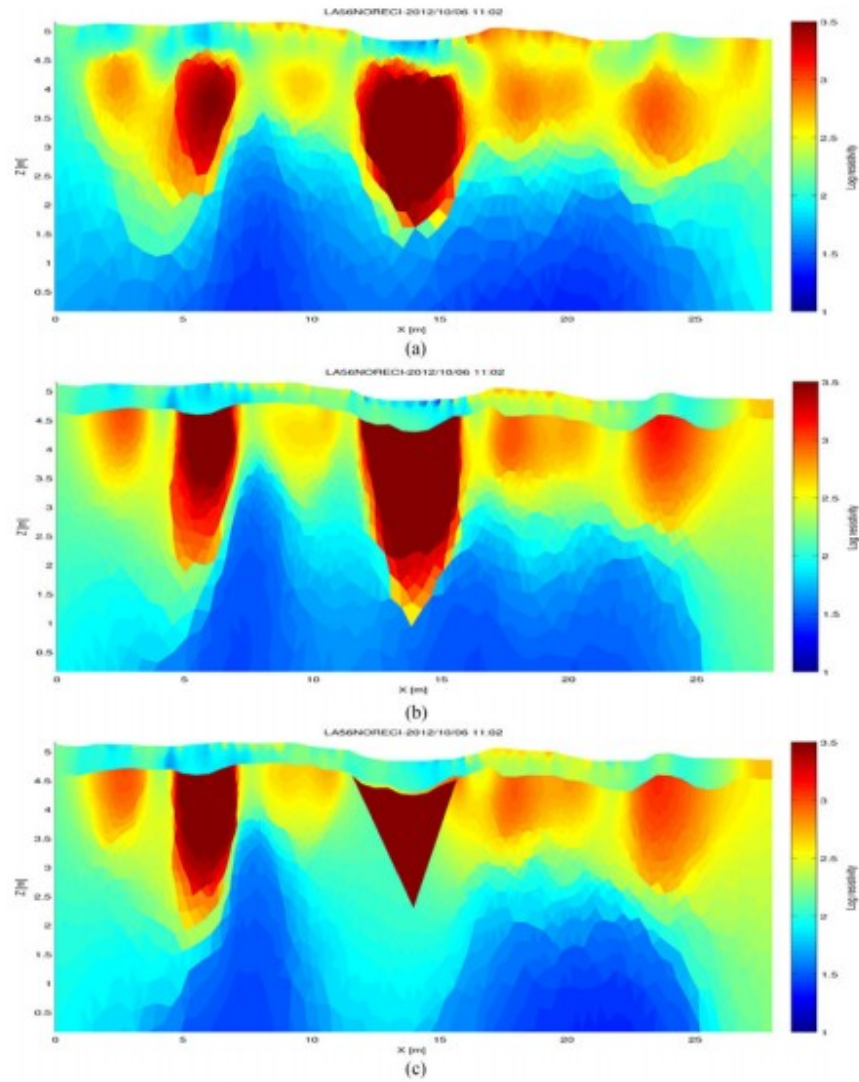


Fig. 7. Line 9 inverted bulk resistivity (ohmmeter) displayed with \log_{10} scales. (a) Unconstrained inversion. (b) Active layer mesh-constrained inversion. (c) Active layer and ice-wedge mesh-constrained inversion.

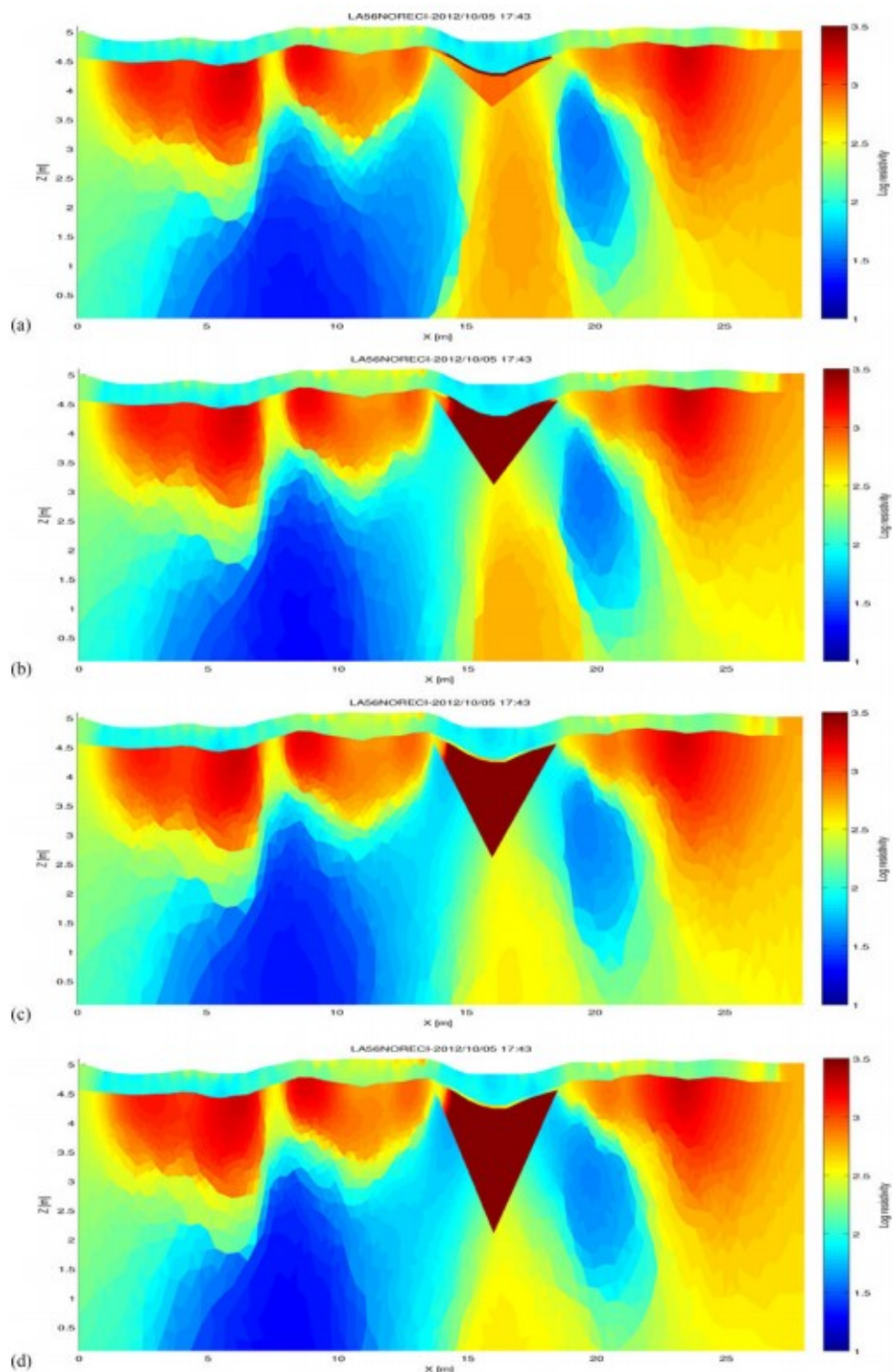


Fig. 8. Line 6 inverted bulk resistivity (ohmmeter) with increasing ice-wedge depth scales. (a) 1 m, (b) 1.5 m, (c) 2 m, and (d) 2.5 m below the base of the active layer.

TABLE I
STATISTICS OF THE INVERSION FOR LINE 6, COMPARISON BETWEEN THE INVERTED AND THE MEASURED RESISTIVITY

Inversion-Type	Mean Absolute \log_{10} difference $< (\log_{10}(\rho_{\text{Measured}}) - \log_{10}(\rho_{\text{Inv}})) >$	Relative Mean Absolute difference $< \left \frac{(\rho_{\text{Measured}} - \rho_{\text{Inverted}})}{(\rho_{\text{Measured}})} \right >$	Root mean squared Error	Relative RMSE
UNconstrained	0.047	0.13	0.096	0.35
ALT-mesh-constrained	0.037	0.100	0.086	0.33
ALT-IW-mesh-constrained-1.00 deep	0.036	0.10	0.085	0.32
ALT-IW-mesh-constrained-1.50 deep	0.036	0.11	0.087	0.34
ALT-IW-mesh-constrained-2.00 deep	0.037	0.10	0.085	0.32
ALT-IW-mesh-constrained-2.50 deep	0.036	0.1	0.085	0.32

ρ stands for apparent resistivity (ohmmeter). "UNconstrained" means: Inversion without any mesh constrain. "ALT-mesh-constrained" means: Inversion with the active layer depth taken into account in the mesh generation. "ALT-IW-mesh-constrained-XX deep" means: mesh generated with active layer depth and ice-wedge constraints and bottom of the ice wedge is at XX meter depth.

TABLE II
STATISTICS OF THE INVERSION FOR LINE 9, COMPARISON BETWEEN THE INVERTED AND THE MEASURED RESISTIVITY

Inversion-Type	Mean Absolute \log_{10} difference $< (\log_{10}(\rho_{\text{Measured}}) - \log_{10}(\rho_{\text{Inv}})) >$	Relative Mean Absolute difference $< \left \frac{(\rho_{\text{Measured}} - \rho_{\text{Inverted}})}{(\rho_{\text{Measured}})} \right >$	Root mean squared Error	Relative RMSE
UNconstrained	0.024	0.062	0.045	0.14
ALT-mesh-constrained	0.017	0.041	0.024	0.06
ALT-IW-mesh-constrained	0.015	0.0215	0.021	0.053

ρ stands for apparent resistivity (ohm.m). "UNconstrained" means: Inversion without any mesh constrain. "ALT-mesh-constrained" means: Inversion with the active layer depth taken into account in the mesh generation. "ALT-IW-mesh-constrained" means: mesh generated with active layer depth and ice-wedge constrained.

By visual inspection, we see that the inversions without GPR constraints reveal three resistive zones, with the highest resistivity zone corresponding to the presence of an ice wedge. This is consistent with the radargram presented in Figs. 1(e) and 5 (f). Furthermore, while ERT data show a decrease in resistivity in the permafrost due to the increase in salinity and unfrozen water content, GPR data do not show any reflector there and thus confirms that such a change is likely gradual. On line 6 and more strongly on line 9, the presence of another ice wedge at around 5 m is also evident. By using the GPR slices, we see that the ice wedges connect between these two lines.

Comparing the three different types of inversion on Figs. 6 and 7 shows that applying constraints on the ERT inversion mesh does not influence the large-scale structure in the ERT but still has significant impact on small-scale variability. However, constraining the ALT in the inversion mesh leads to significant changes in the estimated distribution of electrical resistivity in the active layer as well as the shape of the ice wedge. Looking at the relative mean absolute difference between simulated and measured data for the various types of inversions shows that constraining the ALT position slightly decreases the model-data misfit and helps to constrain the shape of the ice wedge in the ERT profile. The obtained model also looks more realistic with regard to the distribution of electrical conductivity. In particular, we know from soil cores at the NGE site that permafrost below ice wedge tends to be saline and thus expect a strong contrast at the bottom of the ice wedge. However, the inversion performed with both active layer and ice-wedge constraints shows no substantial improvement in terms of the misfit. These results show that constraining the ERT mesh with the ALT obtained from the

GPR data is valuable, while the value of constraining the geometry of the ice wedge cannot be yet assessed.

Fig. 8(a)–(c) depicts different mesh-constrained inversions along line 6, where both the active layer and the ice wedge are constrained with GPR data from Fig. 5(a) and (f), but where different depths of the ice wedge are evaluated. The corresponding statistics are presented in Table I in the third to sixth rows. Results show that constraining the ERT with an inaccurately sized ice wedge mesh adversely affects the inversion; the inversion results were better when no constraints were used instead of an incorrect ice-wedge constraint [Fig. 8(a) to be compared with Fig. 6(b)]. We think that the incorrect ice-wedge depth picked from the GPR data for line 6 is mainly due to a large uncertainty in the velocity estimation, possibly due to the silt layer above the ice wedge, which was thinner for line 9. The last inversion, which includes a thicker ice wedge within the saline permafrost on line 9, appears to give more realistic results. Overall, mesh-constrained inversion can improve the subsurface imaging but ensuring the accuracy of the structural constraints is critical.

SECTION V.

Conclusion

Through field data analysis and numerical modeling, we investigated what type of information can be quantitatively and reliably extracted from GPR data in an ice-wedge dominated Arctic tundra study site and explored the influence of a freeze-thaw condition during different seasons on the GPR signal. Results show that GPR data collected during the growing season enables reliable estimates of thaw layer thickness with associated uncertainty mainly related to spatial variability in the volumetric fractions of porosity, organic, and mineral components and most importantly water content. We also found that frozen season GPR data are very useful for estimating snow depth, ALT, and the vertical and lateral extents of ice wedges. This finding offers potential to rapidly characterize permafrost systems with the GPR during the frozen season, when the GPR signal-to-noise ratio is higher, and when data can be easily collected with a snow mobile and with less disturbance to the ecosystem than during the growing season. In general, probe-, GPR-, and ERT-based measurements show good agreement and provide complementary information about the ALT and conductivity, the ice-wedge lateral dimensions, and depth. A numerical study of GPR signatures during frozen season conditions confirms that GPR hyperbolas correspond to the lower corner of the ice wedges, and that the top of the ice wedge is difficult to identify due to its close proximity (< 25 cm) below the base of the active layer. The GPR-derived ice-wedge structural information can be used to constrain ERT inversion and better define the active layer and ice-wedge resistivity and their dimension. These results pave the way to coupled ERT and GPR inversion for improved imaging of subsurface properties over space and time in the Arctic tundra.

REFERENCES

- [1] P. Friedlingstein et al., "Climate-carbon cycle feedback analysis: Results from the C(4)MIP model intercomparison," *J. Climate*, vol. 19, no. 14, pp. 3337–3353, 2006. [2] J. H. Bradford, J. P. McNamara, W. Bowden, and M. N. Gooseff, "Measuring thaw depth beneath peat-lined arctic streams using ground-penetrating radar," *Hydrol. Process.*, vol. 19, pp. 2689–2699, 2005. [3] S. S. Hubbard et al., "Quantifying and relating land-surface and subsurface variability in permafrost environments using Lidar and surface geophysical datasets," *Hydrogeol. J.*, vol. 21, pp. 149–169, 2013. [4] S. A. Arcone, D. E. Lawson, A. J. Delaney, J. C. Strasser, and J. D. Strasser, "Ground-penetrating radar reflection profiling of groundwater and bedrock in an area of discontinuous permafrost," *Geophysics*, vol. 63, pp. 1573–1584, 1998. [5] S. A. Arcone, P. V. Sellman, and A. J. Delaney, "Radar detection of ice wedges in Alaska," *Cold Regions Res. Eng. Lab.*, Hanover, NH, USA, Rep. 82-43.1982, 1982. [6] D. Fortier and M. Allard, "Late Holocene syngenetic ice-wedge polygons development, Bylot Island, Canadian Arctic Archipelago," *Can. J. Earth Sci.*, vol. 41, pp. 997–1012, 2004. [7] K. M. Hinkel et al., "Detection of subsurface permafrost features with ground-penetrating radar, Barrow, Alaska," *Permafrost Periglacial Processes*, vol. 12, pp. 179–190, 2001. [8] T. Watanabe, N. Matsuoka, and H. H. Christiansen, "Ice- and soil-wedge dynamics in the Kapp Linn area, sValbard, investigated by two- and threedimensional GPR and ground thermal and acceleration regimes," *Permafrost Periglacial Processes*, vol. 24, pp. 39–55, 2013. [9] J. S. Munroe et al., "Application of ground-penetrating radar imagery for three-dimensional visualisation of near-surface structures in ice-rich permafrost, Barrow, Alaska," *Permafrost Periglacial Processes*, vol. 18, pp. 309–321, 2007. [10] C. M. Steelman, A. L. Endres, and J. van der Kruk, "Field observations of shallow freeze and thaw processes using high-frequency groundpenetrating radar," *Hydrol. Processes*, vol. 24, pp. 2022–2033, 2010. [11] A. Gusmeroli, L. Liu, K. Schaefer, T. Zhang, T. Schaefer, and G. Grosse, "Active layer stratigraphy and organic layer thickness at a thermokarst site in arctic alaska identified using ground penetrating radar," *Arctic, Antarctic, Alpine Res.*, vol. 47, pp. 195–202, 2015. [12] Loisel, Z. Yu, A. Parsekian, J. Nolan, and L. Slater, "Quantifying landscape morphology influence on peatland lateral expansion using groundpenetrating radar (GPR) and peat core analysis," *J. Geophys. Res., Biogeosci.*, vol. 118, pp. 373–384, 2013. [13] H. Wainwright, A. Liljedahl, B. Dafflon, C. Ulrich, J. Peterson, and S. Hubbard, "Mapping snow depth within a tundra ecosystem using multiscale observations and Bayesian methods," *Cryosphere*, vol. 11, pp. 857– 875, 2017. [14] J. H. Bradford, J. T. Harper, and J. Brown, "Complex dielectric permittivity measurements from ground-penetrating radar data to estimate snow liquid water content in the pendular regime," *Water Resour. Res.*, vol. 45, pp. 373– 384, 2009. [15] P. Hoekstra, P. V. Sellmann, and A. Delaney, "Ground and airborne resistivity surveys of permafrost near Fairbanks, Alaska," *Geophysics*, vol. 40, no. 4, pp. 641–656, 1975. [16] K. Yoshikawa, V. Romanovsky, N. Duxbury, J. Brown,

and A. Tsapin, "The use of geophysical methods to discriminate between brine layers and fresh-water taliks in permafrost regions," *J. Glaciol. Geocryol.*, vol. 26, pp. 301–309, 2004. [17] P. P. Overduin, S. Westermann, K. Yoshikawa, T. Haberlau, V. Romanovsky, and S. Wetterich, "Geoelectric observations of the degradation of nearshore submarine permafrost at Barrow (Alaskan Beaufort Sea)," *J. Geophys. Res., Earth Surf.*, vol. 117, no. F2, pp. 1–9, 2012. [18] T. R. Brosten et al., "Profiles of temporal thaw depths beneath two arctic stream types using ground-penetrating radar," *Permafrost Periglacial Processes*, vol. 17, pp. 341–355, 2006. [19] J. Mackay and C. Burn, "The first 20 years (1978-1979 to 1998-1999) of ice-wedge growth at the Illisarvik experimental drained lake site, western Arctic coast, Canada," *Can. J. Earth Sci.*, vol. 39, no. 1, pp. 95–111, 2002. [20] S. Muster, M. Langer, B. Heim, S. Westermann, and J. Boike, "Subpixel heterogeneity of ice-wedge polygonal tundra: A multi-scale analysis of land cover and evapotranspiration in the Lena River Delta, Siberia," *Tellus B*, vol. 64, 2012. [21] A. Liljedahl, L. Hinzman, and S. Jorg, "Ice-wedge polygon type controls low-gradient watershed-scale hydrology," in *Proc. 10th Int. Conf. Permafrost*, 2012, vol. 1, pp. 231–236. [22] A. K. Liljedahl et al., "Pan-arctic ice-wedge degradation in warming permafrost and its influence on tundra hydrology," *Nature Geosci.*, vol. 9, pp. 312–318, 2016. [23] B. Dafflon et al., "Geophysical estimation of shallow permafrost distribution and properties in an ice-wedge polygon-dominated arctic tundra region," *Geophysics*, vol. 81, no. 1, pp. WA247–WA263, 2016. [24] G. Niu and Z. Yang, "Effects of frozen soil on snowmelt runoff and soil water storage at a continental scale," *J. Hydrometeorol.*, vol. 7, no. 5, pp. 937–952, 2006. [25] T. Osterkamp and M. Jorgenson, "Permafrost conditions and processes," in *Geological Monitoring*. Boulder, CO, USA: Geol. Soc. Amer., 2009, pp. 205–227. [26] J. Stockwell, "The CWP/SU: Seismic Unix package," *Comput. Geosci.*, vol. 25, pp. 415–419, 1999. [27] A. Giannopoulos, "Modelling ground-penetrating radar by GprMax," *Construct. Build. Mater.*, vol. 19, no. 10, pp. 755–762, 2005. [28] C. Warren, A. Giannopoulos, and I. Giannakis, "gprMax: Open source software to simulate electromagnetic wave propagation for ground penetrating radar," *Comput. Phys. Commun.*, vol. 209, pp. 163–170, 2016. [29] N. R. Peplinski, F. T. Ulaby, and M. C. Dobson, "Dielectric properties of soils in the 0.3-1.3-GHz range," *IEEE Trans. Geosci. Remote Sens.*, vol. 33, no. 3, pp. 803–807, May 1995. [30] C. Rucker, T. G. G. uthner, and K. Spitzer, "3-d modeling and inversion of DC resistivity data incorporating topography—Part I: Modeling," *Geophys. J. Int.*, vol. 166, pp. 495–505, 2006. [31] T. G. C. Rucker and K. Spitzer, "3-d modeling and inversion of DC resistivity data incorporating topography—Part II: Inversion," *Geophys. J. Int.*, vol. 166, pp. 506–517, 2006. [32] C. Geuzaine and J. Remacle, "Gmsh: A three-dimensional finite element mesh generator with built-in pre- and post-processing facilities," *Int. J. Numer. Methods Eng.*, vol. 79, pp. 1309–1331, 2009. [33] H. Si, "TetGen, a Delaunay-based tetrahedral mesh generator," *ACM Trans. Math. Softw.*, vol. 41, no. 2, pp. 1–36, 2015. [34] J. R. Shewchuk, "Delaunay refinement algorithms for triangular mesh generation," *Comput.*

Geom., Theory Appl., ACM Trans. Math. Softw., vol. 22, nos. 1-3, pp. 21-74, 2002. [35] E. Slob and J. Fokkema, "Coupling effects of two electric dipoles on an interface," Radio Sci., vol. 37, no. 5, pp. 1-10, Oct. 2002.